Chem. Eng. Sci. **64**, *4488-4497 (2009);* http://dx.doi.org/10.1016/j.ces.2008.11.028

A particle-based model for the transport of erythrocytes in capillaries

By S. Majid Hosseini[1] and James J. Feng[1,2]†

[1]Department of Chemical and Biological Engineering, University of British Columbia, Vancouver, BC V6T 1Z3, Canada

[2]Department of Mathematics, University of British Columbia, Vancouver, BC V6T 1Z2, Canada

This paper presents a two-dimensional particle-based model for the red blood cell, and uses it to compute cell deformation in simple shear and pressure-driven flows. The cell membrane is replaced by a set of discrete particles connected by nonlinear springs; the spring law enforces conservation of the membrane area to a high accuracy. In addition, a linear bending elasticity is implemented using the deviation of the local curvature from the innate curvature of the biconcave shape of a resting red blood cell. The cytoplasm and the external liquid are modeled as homogeneous Newtonian fluids, and discretized by particles as in standard smoothed-particle-hydrodynamics (SPH) solution of the Navier-Stokes equations. Thus, the discrete particles serve not only as a numerical device for solving the partial differential equations, but also as a means for incorporating microscopic physics into the model. Numerically, the fluid flow and membrane deformation are computed, via the particle motion, by a two-step explicit scheme. The model parameters are determined from experimental measurements of cell viscosity and elastic moduli for shear, areal dilatation and bending. In a simple shear flow, the cell typically deforms to an elongated shape, with the membrane and cytoplasm undergoing tank-treading motion. In a Poiseuille flow, the cell develops the characteristic parachute shape. These are consistent with experimental observations. Comparison with prior computations using continuum models shows quantitative agreement without any fitting parameters, which is taken to be a validation of the particle-based model and the numerical algorithm.

1. Introduction

Several human diseases are caused by pathological changes in the mechanical properties of cells (Suresh *et al.* 2005; Lee & Lim 2007). In malaria, the changes are brought on by external factors such as parasites and bioactive lipids. In cancer, the changes are due to internal factors (genetic mutation). These factors change the internal structure and mechanical behavior of living cells through biochemical reactions. The disease progression is often facilitated by altering in mechanical behavior of living cells such as large changes of elastic modulus. For instance, the Young's modulus of cancerous cells is about one-tenth that of healthy cells (Lee & Lim 2007). This will increase the deformability of cancerous cells so they can migrate through size-limited pores in the basal membrane and endothelium during metastasis. Healthy red blood cells (RBCs) squeeze through tiny capillaries to deliver oxygen to various parts of the body. When they are infected by the protozoan Plasmodium falciparum, intracellular structural changes may increase the elastic modulus of the red cell by more than a factor of 10 (Suresh 2006). The stiffened

† Corresponding author. E-mail jfeng@CHBE.UBC.CA

RBCs can no longer deform sufficiently to traverse narrow capillaries. Instead they block the capillaries and disrupt the blood flow, possibly leading to coma and even death.

Studying the exact changes in mechanical behavior of infected cells illuminates the mechanism behind disease progression and provides important knowledge in the fight against these diseases. By understanding the alteration in mechanical behavior of infected cells it will be possible to design new diagnostic devices and techniques to detect diseases in an early stage. For interpreting and predicting the mechanical behavior of living cells, theoretical modeling has followed two main directions: the *continuum* approach and the *microstructural* approach (Lim *et al.* 2006).

The continuum approach treats the whole cell or its components as homogeneous materials represented by appropriate constitutive equations. The relevant model parameters are determined from experimental observations and measurements. The simplest continuum model is the Newtonian liquid drop model (Yeung & Evans 1989; Drury & Dembo 1999), which treats the cell as a liquid drop with a constant cytoplasmic viscosity and a constant surface tension, the latter representing cell membrane elasticity. More complex constitutive equations, accounting for shear-thinning and viscoelasticity, e.g., have also been proposed. Still more sophisticated continuum models seek to reflect the multiphase nature of the cellular components, either through mixture-type "biphasic models" (Herant *et al.* 2003) or an explicitly two-phase treatment of the cell as a deformable capsule, with liquid cytoplasm enclosed by an elastic or viscoelastic membrane. The latter approach is related to fluid-structure interactions in mechanical systems, and thus is especially appealing to fluid dynamicists (Eggleton & Popel 1998; Pozrikidis 2005*b*; Li & Sarkar 2008; Pappu & Bagchi 2008; Pan & Wang 2008).

The advantage of the continuum models is that they are amenable to computational methods developed for fluid and solid mechanics. However, they do not reflect the microstructural changes inside the cell that sometimes take place in response to mechanical stimulation. One example is the activation of white blood cells, which may drastically alter the cells' mechanical properties (Yap & Kamm 2005*a*,*b*). Such changes cannot be faithfully represented by, say, the relaxation time of a viscoelastic model of leukocytes (Dong & Skalak 1992).

The microstructural models seek to account for the interplay between microstructural remodeling inside the cell and its mechanical behavior as a whole. So far, the most popular and successful models are the *network* models, which treat the cytoskeleton as the main structural component of the cell that determines its mechanics. For instance, Stamenovic & Coughlin (2000) modeled the elastic response of the cell by a network of struts and cables that represent the microtubules and actin filaments. Boey *et al.* (1998) proposed a three-dimensional network model inspired by the spectrin network in erythrocytes. An elastically based network free energy may then be minimized to determine the equilibrium shape of the red cell, as well as its deformation subject to external stretching (Li *et al.* 2005). Allowing the cytoskeletal network to undergo active polymerization, Herant *et al.* (2003) incorporated the kinetics and network-membrane interaction through convection-diffusion equations. Here, the network is described as a pseudo-continuum having statistic properties. One obvious advantage of network models is the knowledge, to a certain degree of approximation, of the configuration of the intracellular components. If the network is discrete with a large but finite number of links, that physical discretization can be used directly as a numerical discretization for computation (Bottino 1998; Secomb *et al.* 2007).

Recently, several research groups have experimented with *particle-based representations* of cells, and proposed what may be seen as a new class of discrete microstructural models. Boryczko *et al.* (2003) and Dzwinel *et al.* (2003) treated an erythrocyte as an elastic object of uniform properties, which is represented by a rectangular lattice of particles connected

by elastic springs. Postulating conservative and dissipative forces among particles of the same (liquid-liquid or solid-solid) and different (solid-liquid) species, they solved for the flow of the suspending plasma and the solid deformation by a variant of the dissipative particle dynamics (DPD) method. Inspired by the smoothed particle hydrodynamics (SPH) method, Tanaka & Takano (2005) and Tsubota *et al.* (2006*a*,*b*) represented the cell membrane by particles connected by springs that produce resistance to both stretching and bending. With the fluid particles exerting forces on the membrane particles, the motion and deformation of the cell can be computed using SPH algorithms. Most recently, Pivkin & Karniadakis (2008) presented a three-dimensional DPD model for RBCs based on coarse-graining the spectrin network models.

Obviously, the discrete particle models are in their infancy and not nearly as sophisticated as the network models. In fact, one can easily point out several flaws with these models. For example, treating the whole cell as a homogeneous lattice (Dzwinel *et al.* 2003) makes it impossible to account for any organelle in the cytoplasm, much less dynamic changes of the microstructure as happen during neutrophil activation. In this sense, the cell is more like an elastic continuum. Besides, the effective elasticity of the lattice depends not only on the spring constant, but also on the specific shape, size and topology of the grid. This makes it difficult to compare between different models and with experiments. The SPH-based models are flawed in their representation of membrane-fluid interaction. The model of Tsubota *et al.* (2006*a*) does not have any cytoplasm at all, and thus one cannot speak of conserving the cell volume or mass. Instead an ad hoc constraint is placed on the overall area (or arc length in 2D) of the membrane to discourage severe expansion or contraction of the cell. The model of Tanaka & Takano (2005) includes the cytoplasm, but it tends to leak through the membrane. Apparently the inter-particle forces are not properly designed (Nakamura *et al.* 2006). Moreover, the particle-level model parameters have not been systematically related to physiological measurements; they have to assume unrealistic values for the prediction to be quantitatively comparable with reality (Tanaka & Takano 2005).

In spite of these problems, we see a unique potential for discrete particle models. In comparison with the network, the particles offer far more freedom in modeling the internal structure of cells. For instance, clusters of particles having common properties that differ from the surroundings may represent various organelles, and the interaction among different particles may be dynamically evolved to reflect, say, the remodeling of the cytoskeleton triggered by internal or external factors as alluded to at the beginning. From a computational standpoint, particle methods are meshless, and particularly suitable for simulating large deformation of soft matter. Thus, it seems worthwhile to develop the ideas of discrete particle models further, and potentially into a tool for studying the structural-property-disease coupling that sometimes comes under the name of nanobiomechanics (Lee & Lim 2007).

This paper represents a first step in that direction. We adapt the SPH picture of particles, which have overlapping regions of influence for smoothing and interpolation, by adding extensional and bending elasticity between the particles representing the RBC membrane. As indicated above, the discrete nature of the model allows one to go beyond the continuum framework to probe micro- and nanostructural responses to external stimulation. However, we limit ourselves in this paper to establishing a basic cell model without active reconfiguration of the microstructures. These features will be incorporated in future studies. Thus, we set two objectives for this work: (*a*) to present a 2D particle-based model for the erythrocyte with a Newtonian-liquid cytoplasm and an elastic membrane having both extensional and bending moduli; (*b*) to validate this model by computing RBC motion and deformation in 2D shear and pressure-driven flows, and

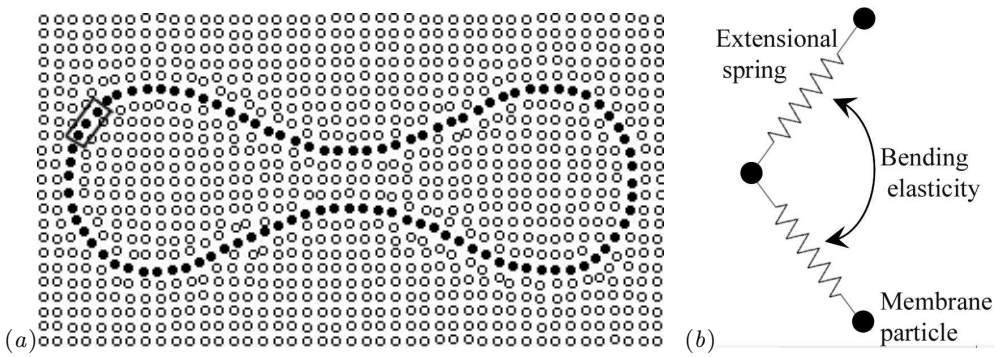

FIGURE 1. (a) Particle-based model for the red blood cell, with fluid particles representing the cytoplasm and the suspending plasm, and spring-connected solid particles representing the cell membrane. (b) Schematic of extensional and bending elasticity between particles in the membrane.

comparing the numerical predictions to experimental data and continuum-based computations in the literature.

2. Physical model and numerical scheme

Consider an RBC suspended in a Newtonian plasma. Similar to previous discrete-particle models, we deal only with 2D planar geometry here, and leave the extension to 3D to a future endeavor. We view the RBC as a capsule made of an elastic membrane enclosing a Newtonian cytoplasm. The plasma and the cytoplasm flow according to the Navier-Stokes equations. Thus each is discretized by "fluid particles" in the SPH sense, the two kinds having different properties tuned to reflect the density and viscosity of the two liquids. The membrane is replaced by a collection of "solid particles", connected by elastic springs obeying a nonlinear spring law (Fig. 1). In addition, we introduce a separate bending elasticity that controls the variation of the membrane curvature. Note that in 2D, shearing in the tangential plane of the membrane is excluded; membrane deformation is limited to stretching and compression tangential to the membrane and bending.

It seems appropriate at this point to briefly review the ideas underlying the SPH method and clarify the relationship between these and our cell model. SPH originated in astrophysics some three decades ago (Gingold & Monaghan 1977; Lucy 1977), and was later adapted for solving hydrodynamic problems (Morris *et al.* 1997). In this form, SPH is mostly a numerical device for discretizing the Navier-Stokes equations in Lagrangian coordinates. The particles are interpolation points from which the fluid properties may be calculated by "smoothing" over neighboring particles. Although the particles have mass and move according to Newton's law of motion, the forcing terms stem directly from discretizing the continuum governing equations. Solid boundaries are discretized by solid particles, and the fluid-solid interaction may be defined so as to satisfy the no-slip boundary condition. Being completely meshless, the method does not require connectivity data as do finite volume and finite element methods. Thus, SPH is convenient in dealing with complex flows exhibiting large deformations, and especially fluid-solid interactions with large interfacial deformation (Hosseini & Amanifard 2007).

In our cell model of Fig. 1, the fluid components inside and outside the membrane are represented by classical SPH particles. For the membrane particles, however, we insert additional physics on the particle level in the form of elastic forces that on the cell level

amount to the appropriate elastic properties of the membrane. Specifically, we introduce a set of nonlinear springs between each pair of neighboring particles on the membrane to account for compression and stretching (Fig. 1*b*). The spring law, to be detailed in the following, reflects the areal conservation and strain-hardening nature of the RBC membrane (Skalak *et al.* 1973). In addition, we introduce a bending elasticity that penalizes deviations of the local curvature from that of the biconcave "resting shape" of RBCs. This way, the particles representing the membrane not only play their conventional role in SPH as interpolating points, but also carry new physics that define membrane elasticity. As mentioned above, it is the latter role that makes the discrete-particle approach particularly suitable for modeling the coupling between cell mechanics and microstructural evolution inside the cell.

2.1. *Constitutive models for the membrane*

The lipid-bilayer structure of the red blood cell membrane endows it with a very high modulus against areal expansion or contraction, so the surface area is essentially conserved (Skalak *et al.* 1973; Eggleton & Popel 1998). In the meantime, the membrane is very flexible with respect to shear deformation and bending, such that the RBC can deform readily to pass through narrow capillaries. The membrane is so thin compared with the cell size that it may be considered a 2D elastic shell. A constitutive equation for such a membrane can be obtained by adapting 3D elasticity or by postulating a 2D relationship directly. Barthès-Biesel *et al.* (2002), among others, have compared the constitutive equations that have been proposed for RBC membrane. The 2D version of Hooke's law is the simplest constitutive law; it assumes a linear dependence of tension on surface deformations, and is applicable only for small deformations. The neo-Hookean and Mooney-Rivlin models are classical hyperelastic models for rubber-like materials. But their lack of membrane areal conservation and strain-softening behavior for large deformation make them inappropriate for RBC membrane modeling (Barthès-Biesel *et al.* 2002).

So far, the most successful constitutive model for RBC membranes appears to be that of Skalak *et al.* (1973). When a 2D elastic shell is subject to in-plane stretching, with extensional ratio λ_1 and λ_2 along the principal directions, Skalak *et al.* (1973) proposed the following strain-energy function:

$$W_S = \frac{E_S}{4}\left(\frac{1}{2}I_1^2 + I_1 - I_2\right) + \frac{E_D}{8}I_2^2, \tag{2.1}$$

where E_S and E_D are the shear and dilatation modulus of the membrane, and the strain invariants $I_1 = \lambda_1^2 + \lambda_2^2 - 2$ and $I_2 = \lambda_1^2\lambda_2^2 - 1$. The extensional stress components in the membrane follow from W_S:

$$T_1 = \frac{\lambda_1}{\lambda_2}\left[\frac{E_S}{2}\left(\lambda_1^2 - 1\right) + \frac{E_D}{2}\lambda_2^2\left(\lambda_1^2\lambda_2^2 - 1\right)\right], \tag{2.2}$$

$$T_2 = \frac{\lambda_2}{\lambda_1}\left[\frac{E_S}{2}\left(\lambda_2^2 - 1\right) + \frac{E_D}{2}\lambda_1^2\left(\lambda_1^2\lambda_2^2 - 1\right)\right]. \tag{2.3}$$

Any changes in the area produces a deviation of $\lambda_1\lambda_2$ from unity, which will result in a large elastic tension due to the large magnitude of E_D relative to E_S. As a result, the membrane area is kept approximately constant during deformation. In addition, the Skalak constitutive model exhibits strain-hardening for large deformation (Barthès-Biesel *et al.* 2002). Based on these features, we have decided to adopt the Skalak constitutive model for the extensional springs in our particle model.

In our 2D simulation, the RBC membrane is a closed planar curve instead of a 2D

curved surface. By putting the out-of-plane stress component T_2 to zero, one obtains an expression of λ_2 in terms of λ_1. When plugged into Eq. (2.2), this yields the one-dimensional stress for stretching the membrane (Barthès-Biesel *et al.* 2002):

$$T = \frac{E_S}{2}\lambda_1(\lambda_1^2 - 1)\sqrt{\frac{1 + C\lambda_1^4}{1 + C\lambda_1^2}}\left[1 + \frac{C(1 + C\lambda_1^2)}{(1 + C\lambda_1^4)^2}\right], \tag{2.4}$$

where $C = E_D/E_S$, the ratio between the dilatation and shear moduli, is above 10^4 for healthy RBC (Skalak *et al.* 1973). For our extensional springs between the membrane particles, λ_1 will be the ratio between the deformed and resting lengths.

The bending elasticity is reflected by a resistance against deviation from the equilibrium membrane curvature corresponding to the biconcave natural shape of the RBC. Following Evans & Fung (1972), we describe this biconcave shape by the following equation:

$$\bar{y} = 0.5\,(1 - \bar{x}^2)^{1/2}(c_0 + c_1\bar{x}^2 + c_2\bar{x}^4), \quad -1 \le \bar{x} \le 1, \tag{2.5}$$

where $c_0 = 0.207$, $c_1 = 2.002$, $c_2 = 1.122$, and the non-dimensional coordinates $(\bar{x}, \bar{y})$ are scaled by the radius of a human RBC $a = 3.9$ μm.

Almost all prior continuum models for the RBC membrane have used a linear bending elasticity (Pozrikidis 2003; Bagchi 2007; Zhang *et al.* 2007):

$$m = E_B(\kappa - \kappa_0), \tag{2.6}$$

where m is an external bending moment exerted on a infinitesimal segment of the membrane, E_B is the bending modulus, and κ and κ_0 are the local curvature in the deformed and resting states. The sign conventions for m and κ are that m is positive if it squeezes the outside of the membrane and stretches the inside, and κ is positive if the membrane is locally concave, with the center of the osculating circle lying outside the cell. This is the case at the center of the RBC, while near the edge $\kappa < 0$. To implement Eq. (2.6) for our particle-based membrane, κ will be computed from the position of neighboring particles and m must be converted to nodal forces. Details will be given below in subsection §2.5.

2.2. *Governing equations for fluid flow*

In the SPH algorithm, incompressibility is approximated by a small artificial compressibility. Thus, the governing equations may be written in a Lagrangian framework as:

$$\frac{D\rho}{Dt} = -\rho\nabla\cdot\boldsymbol{v}, \tag{2.7}$$

$$\frac{D\boldsymbol{v}}{Dt} = \boldsymbol{g} + \frac{1}{\rho}\nabla\cdot\boldsymbol{\tau} - \frac{1}{\rho}\nabla p, \tag{2.8}$$

$$p = p_0\left[\left(\frac{\rho}{\rho_0}\right)^{\gamma} - 1\right], \tag{2.9}$$

where t is time, $\boldsymbol{g}$ is the gravitational acceleration, p is pressure, $\boldsymbol{v}$ is the velocity vector, $\boldsymbol{\tau}$ is the viscous stress tensor and D/Dt refers to the material derivative. Although body force will not be important for the computations to be presented here, we will include $\boldsymbol{g}$ in discussing the algorithm for completeness.

The artificial compressibility is a device for coupling the particle pressure to their motion (Monaghan 1992). The motion of particles, if not observing the constraint $\nabla\cdot\boldsymbol{v} = 0$, produces a variation in the particle density ρ through Eq. (2.7). In turn, this causes a pressure disturbance through the artificial equation of state (Eq. 2.9), which can then be used to correct the velocity field and make it solenoidal. In the equation of state

(Batchelor 1999), ρ_0 and p_0 are reference quantities, and the large exponent $\gamma = 7$ produces a strong pressure response to density variations and keeps the density variations negligibly small (below 1%), even at high Reynolds numbers (Morris *et al.* 1997; Cleary *et al.* 2002).

2.3. *Discretization using SPH*

The SPH method allows any function to be interpolated from its values at a set of discrete points—the SPH particles—using a kernel or weighting function $W(\boldsymbol{r} - \boldsymbol{r}', h)$, which specifies the contribution to any field variable at $\boldsymbol{r}$ by a particle at $\boldsymbol{r}'$ that lies within $2h$ of $\boldsymbol{r}$. The weighting function is normalized such that (Monaghan 1992)

$$\int_V W(\boldsymbol{r} - \boldsymbol{r}', h) d\boldsymbol{r}' = 1, \qquad \lim_{h \to 0} W(\boldsymbol{r} - \boldsymbol{r}', h) = \delta(\boldsymbol{r} - \boldsymbol{r}'), \tag{2.10}$$

V being the entire space. If a field variable $A(\boldsymbol{r})$ is known only at a discrete set of particles $\boldsymbol{r}'_j$, then its value at any spatial location $\boldsymbol{r}$ can be approximated by:

$$\begin{aligned} < A_h(\boldsymbol{r}) > &= \int_V A(\boldsymbol{r}') W(\boldsymbol{r} - \boldsymbol{r}', h)\, d\boldsymbol{r}' \\ &= \sum_{j=1}^{N} A(\boldsymbol{r}'_j) W(\boldsymbol{r} - \boldsymbol{r}'_j, h) \Delta V_j = \sum_{j=1}^{N} \frac{m_j}{\rho_j} A_j W(\boldsymbol{r} - \boldsymbol{r}'_j, h), \end{aligned} \tag{2.11}$$

where ΔV_j is the volume element at $\boldsymbol{r}'_j$, and has been replaced by the ratio between the mass and density of the jth particle: $\Delta V_j = m_j/\rho_j$. The summation is over all particles that lie within a circle of radius $2h$ centered at $\boldsymbol{r}$, and A_j is a shorthand for $A(\boldsymbol{r}'_j)$.

The gradient $\nabla A(\boldsymbol{r})$ is evaluated through an integration by parts to transfer the gradient operator onto W (Hosseini *et al.* 2007):

$$\nabla A_h(\boldsymbol{r}) = \sum_{j=1}^{N} \frac{m_j}{\rho_j} A_j \nabla W(\boldsymbol{r} - \boldsymbol{r}'_j, h). \tag{2.12}$$

Note that calculating the spatial derivatives in SPH requires no mesh information, and this gives a straightforward way to construct gradient of a function from its values at the SPH particles. In this paper we adopt a popular spline-based kernel function

$$W(\boldsymbol{r}, h) = \frac{\sigma}{h^\nu} \times \begin{cases} 1 - \frac{3}{2}s^2 + \frac{3}{4}s^3 & \text{if } 0 \le s < 1 \\ \frac{1}{4}(2-s)^3 & \text{if } 1 \le s < 2 \\ 0 & \text{if } 2 \le s \end{cases} \tag{2.13}$$

where $s = |\boldsymbol{r}|/h$, ν is the number of dimensions ($\nu = 2$ here) and $\sigma = 2/3$, $10/7\pi$ or $1/\pi$ in one, two and three dimensions, respectively. This kernel has compact support so that its interactions are exactly zero for $r > 2h$. The second derivative of this kernel is continuous and the leading-order error in an interpolation is $O(h^2)$. Higher-order splines can be used, but they interact at larger distances and thus are computationally costlier.

2.4. *Solution algorithm*

Through the interpolation operation outlined above, any partial differential equation can be discretized into ordinary differential equations governing the motion of SPH particles. In particular, the momentum equation (Eq. 2.8) may be discretized for fluid particles as (Monaghan 1992):

$$\frac{D\boldsymbol{v}_i}{Dt} = \boldsymbol{g} - \sum_j m_j \left(\frac{p_i}{\rho_i^2} + \frac{p_j}{\rho_j^2}\right) \nabla_i W_{ij} + \Pi_{ij}, \tag{2.14}$$

where W_{ij} is a shorthand for $W(\boldsymbol{r}_i - \boldsymbol{r}'_j, h)$ and ∇_i designates the derivative with respect to $\boldsymbol{r}_i$. Π_{ij} represents the viscous stress term, and we employ the formula suggested by Morris *et al.* (1997):

$$\Pi_{ij} = \sum_j m_j \frac{(\mu_i + \mu_j)\boldsymbol{r}_{ij} \cdot \nabla_i W_{ij}}{\rho_i \rho_j \, r_{ij}^2} \boldsymbol{v}_{ij}, \tag{2.15}$$

with $\boldsymbol{v}_{ij} = \boldsymbol{v}_i - \boldsymbol{v}_j$, $\boldsymbol{r}_{ij} = \boldsymbol{r}_i - \boldsymbol{r}_j$ and $r_{ij} = |\boldsymbol{r}_{ij}|$ is the distance between particles i and j, whose viscosities μ_i and μ_j may differ if they represent different phases or fluid components.

The momentum equation has three forcing terms on the right-hand-side: body force, the pressure gradient and the viscous force. These must be treated properly, along with the continuity equation and equation of state, to approximate incompressibility. At each time step, the governing equations are solved for each particle to update its position, velocity and pressure. The sequence in which the forcing terms are incorporated can differ from one algorithm to another. Here we use a fully explicit two-step algorithm (Hosseini *et al.* 2007). In the first step, the momentum equation is solved with body force $\boldsymbol{g}$ and viscous force Π but not the pressure gradient. Thus, an intermediate velocity $\tilde{\boldsymbol{v}}$ is generated and the particle positions are updated accordingly. Because this step is not subject to the incompressibility constraint, we expect it to perturb the density of some particles away from the reference value ρ_0. The density variation can be computed directly from the updated particle position (Monaghan 1992)

$$\rho(\boldsymbol{r}) = \sum_j m_j \, W(\boldsymbol{r} - \boldsymbol{r}'_j, h). \tag{2.16}$$

This is equivalent, within the interpolation errors of the scheme, to the continuity equation Eq. (2.7) (Monaghan 1992; Morris *et al.* 1997).

In the second step of the algorithm, the pressure is calculated, using the equation of state (Eq. 2.9), from the perturbed ρ field. Thus, areas with denser particles have a larger ρ and a higher p that would tend to disperse them, and vice versa. The latter action is achieved through correcting the velocity field by solving the momentum equation again, with only the pressure gradient term on the right-hand-side:

$$\hat{\boldsymbol{v}}_i = \sum_j m_j \left(\frac{P_i}{\rho_i^2} + \frac{P_j}{\rho_j^2} \right) \nabla_i W_{ij}. \tag{2.17}$$

For each particle, the velocity $\boldsymbol{v}_i = \tilde{\boldsymbol{v}}_i + \hat{\boldsymbol{v}}_i$ is taken to be the new velocity at the end of the time step, and it should be approximately divergence-free. Finally, the position of the particles are updated by a central differencing scheme:

$$\boldsymbol{r}_i(t + \Delta t) = \boldsymbol{r}_i(t) + \frac{\Delta t}{2}[\boldsymbol{v}_i(t) + \boldsymbol{v}_i(t + \Delta t)]. \tag{2.18}$$

The procedure is repeated for the next time step till a specified time is reached.

Numerical stability of the explicit scheme puts a limit on the time step. The following criterion, due to Morris *et al.* (1997), works well for our computations:

$$\Delta t \leq 0.125 \frac{\rho h^2}{\mu}. \tag{2.19}$$

In addition, SPH algorithms are susceptible to a well-known numerical instability known as the tensile instability, whereby particles tend to form clumps and cause unrealistic fracture in the material when it is being stretched (Monaghan 2005). We suppress this

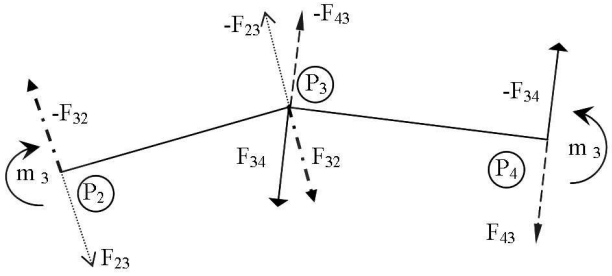

FIGURE 2. Element bending groups (EBGs) used to convert the bending moment to pairs of forces acting on particles in the membrane. The line and arrow styles distinguish pairs of forces used to replace the bending moment on each line segment.

instability by using the scheme of Monaghan (1994), which introduces a small repulsive force between nearby particles when they are in a state of tensile stress.

2.5. *Bending moment*

In representing the bending elasticity in our particle-based model, the moment m needs to be transformed to forces acting on the membrane particles. This is accomplished by using the element bending group (EBG) idea for elastic shells (Zhou & Wagoner 1995). In our 2D membrane, the EBG for a membrane particle is made of two adjacent line segments connecting it to the two neighboring particles. Thus, a membrane with n particles has n line segments and n overlapping EBGs. Figure 2 depicts the EBG centered at membrane particle P_3 that involves 2 line segments connecting 3 membrane particles. At each time step the membrane curvature at each particle is calculated by passing a circle over three neighboring particles. For instance, the curvature at point P_3 will be the inverse of the radius of the circle passing through points P_2, P_3 and P_4. Equation (2.6) then gives the bending moment m_3 at P_3. In the EBG scheme, m_3 acts on both line segments that meet at P_3. For the segment between P_2 and P_3, m_3 is replaced by a pair of equal and opposite forces: $F_{32} = m_3/r_{23}$ on P_3 and $-F_{32}$ on P_2. For the segment between P_3 and P_4, similarly, m_3 generates F_{34} on P_3 and $-F_{34}$ on P_4. This amounts to two forces on P_3. But P_3 is also the end point of two other EBGs centered at P_2 and P_4. Thus, m_2 and m_4 will produce a force $-F_{23}$ and $-F_{43}$, respectively, on P_3. In the end, the particle P_3, and every other membrane particle, receives 4 nodal forces as a result of bending elasticity. Finally, the equation of motion for the membrane particles is:

$$\frac{D\boldsymbol{v}_i}{Dt} = \boldsymbol{g} - \sum_j m_j\left(\frac{p_i}{\rho_i^2} + \frac{p_j}{\rho_j^2}\right)\nabla_i W_{ij} + \Pi_{ij} + \sum_{n=1}^{4} F_{i,n} + \sum_{n=1}^{2} T_{i,n}, \tag{2.20}$$

where the index n refers to neighboring particles on the membrane. This is similar to Eq. (2.14) except for the 4 bending-based nodal forces $F_{i,n}$ and 2 extensional spring forces $T_{i,n}$ along the line segments.

In summary, the main idea underlying our model is the same as in prior models by Tanaka & Takano (2005) and Tsubota *et al.* (2006*b*), which is to produce realistic dynamics on the cell level by manipulating the physics on the particle level. However, our model represents advances beyond prior work in two key aspects: (i) Our model properly implements liquid-membrane interactions, in a way that is consistent with the SPH algorithm. The membrane particles interact with the liquid particles in the cytoplasm and the suspending plasma according to Eq. (2.20), with an inter-particle pressure that moderates the repulsion and attraction between particles. As such, the fluid motion and membrane deformation is fully coupled (Tsubota *et al.* 2006*a*). Moreover, since the mem-

brane particles are held together by extensional elasticity, the particle pressure prevents the fluid particles from leaking through the membrane (Nakamura *et al.* 2006). (ii) We use more realistic constitutive equations for the extensional and bending elasticity, as well as model parameter values that correspond to physiologically realistic values in the literature. As will be shown in the next section, this makes possible direct comparisons with experimental data as well as numerical results based on continuum models. Such comparisons were not possible with the earlier particle models. For instance, Tanaka & Takano (2005) had to treat the membrane bending elasticity as an adjustable parameter when comparing with experiments.

3. Results and analysis

In this section, we study two benchmark problems to demonstrate the capability of our particle-based model: cell deformation in shear flows and Poiseuille flows. The cell deformation can be viewed as the outcome of the competition between viscous forces from the external flow and elastic resistance of the membrane, which is embodied by the dimensionless group

$$G = \frac{\mu U_m}{E_S}, \tag{3.1}$$

where μ is the plasma viscosity, and the characteristic velocity U_m is the mean velocity for a Poiseuille flow and ka for a simple shear at shear rate k, a being the radius of the RBC. G can be likened to the capillary number in drop dynamics (Zhou *et al.* 2008, e.g.). We can also define two ratios between the moduli:

$$\hat{E}_B = \frac{E_B}{a^2 E_S}, \quad C = \frac{E_D}{E_S}. \tag{3.2}$$

Note that in our 2D simulation, E_S and E_D have the dimension of force over length, while E_B has that of energy. The last independent dimensionless group is the Reynolds number

$$Re = \frac{\rho U_m a}{\mu}, \tag{3.3}$$

which is on the order of 10^{-4} for RBC motion in microcirculation as well as in the computations to be described below. Thus, inertia will be negligible.

3.1. *Cell in shear flows*

Fischer *et al.* (1978) observed the deformation of an RBC in simple shear in an experimental setup that keeps the center of the RBC stationary. For sufficiently high shear rates, the cell deforms from its biconcave rest shape to an ellipsoid and then to an elongated spindle-like shape oriented at an angle with the undisturbed flow direction. Meanwhile, the membrane and cytoplasm execute a rotating motion around the center of the cell, which is well known as "tank-treading".

To mimic that experimental setup, we place an RBC in the center of an $8a \times 4a$ rectangular domain with top and bottom walls moving in opposite directions. Periodic boundary conditions are imposed at the left and right boundaries such that particles exiting from one end will emerge from the other. The simulations to be presented use some 12,000 SPH particles in the domain, and 96 particles on the membrane. In this and previous calculations (Hosseini *et al.* 2007), we have confirmed that the spatial resolution is adequate; doubling the number of particles causes a change in the result on the order of 1%.

The computations have used model parameters from physiological data for real human

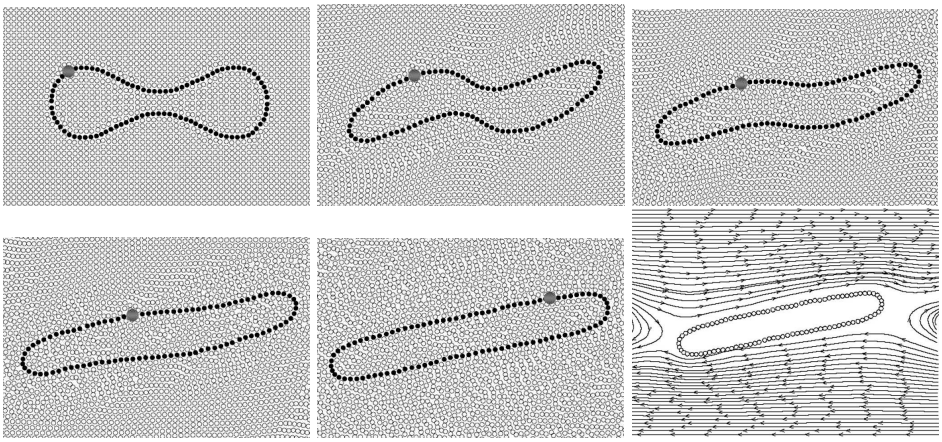

FIGURE 3. Deformation of an RBC in shear flow. $C = 2\times10^4$, $G = 0.234$ and $\hat{E}_B = 2.63\times10^{-3}$. The snapshots are for dimensionless times $kt = 0$, 2, 3, 4 and 10, and the last frame depicts the flow field surrounding the cell in the steady state.

RBC, with $E_S = 5.0 \times 10^{-6}$ N/m, $E_D = 0.1$ N/m and $E_B = 2.0 \times 10^{-19}$ N·m (Skalak *et al.* 1989). The large ratio of $C = 2\times10^4$ ensures that little surface areal dilation occurs and the membrane area is essentially conserved. We have examined differing viscosities for the cytoplasm and the suspending fluid, but the results presented will have equal viscosity for the two liquids: $\mu = 6.0 \times 10^{-3}$ Pa·s. These are the baseline parameters for the simulations. We have also systematically varied G and $\hat{E}_B$ to probe the effects of the membrane elasticity; in these exercises $C = 2 \times 10^4$ is kept constant.

Figure 3 depicts a typical simulations by a sequence of snapshots of the particles in the domain. One of the membrane particles is drawn in larger size to serve as a marker to illustrate the tank treading motion. In the final frame, which is essentially steady state, the cell has an aspect ratio of 6.22 and assumes an angle of $\theta = 13^\circ$ with respect to the far-field flow, and exhibits the tank-treading motion. Note that the cell deforms on the flow time scale $1/k$, rather than on a time scale defined by membrane elasticity, say $\mu a^3/E_B$. This is because at $G/\hat{E}_B = 90$, the bending elasticity is overwhelmed by the flow. Indeed, the final shape of the cell is an almost symmetric cigar shape; the native curvature of the membrane is barely manifested. The steady-state circumference of the cell has increased 3.6% from the rest state. The 2D version of the Skalak constitutive law (Eq. 2.4) assumes that in-plane extension is accompanied by out-of-plane contraction. Thus areal conservation does not imply constant circumference of the cell in the plane.

The steady-state configuration of the cell is sensitive to $\hat{E}_B$ and G. Increasing $\hat{E}_B$ amounts to stronger resistance to bending of the membrane. As a result, the deformed shape of the RBC bears a more distinct signature of the biconcave resting shape (Fig. 4). In fact, for higher $\hat{E}_B$ values, the tank-treading amounts to a periodic rather than steady solution; the high curvature at the edge of the undeformed RBC convects around the membrane. At sufficiently large $\hat{E}_B$ (e.g., $\hat{E}_B = 0.262$), tank-treading can no longer be achieved; instead the cell tumbles as if it were a rigid particle. In comparison, the effect of G is less spectacular. Increasing G while keeping all other parameters unchanged tends to increase the aspect of the elongated cell, and decrease its angle of inclination (Fig. 5). Both are rather mild effects as G varies by a factor of 25.

Zhang *et al.* (2007) computed the behavior of an RBC in simple shear using a continuum model. The membrane is treated as a neo-Hookean viscoelastic material, and the fluid-membrane interaction is accounted for by the immersed boundary method. Al-

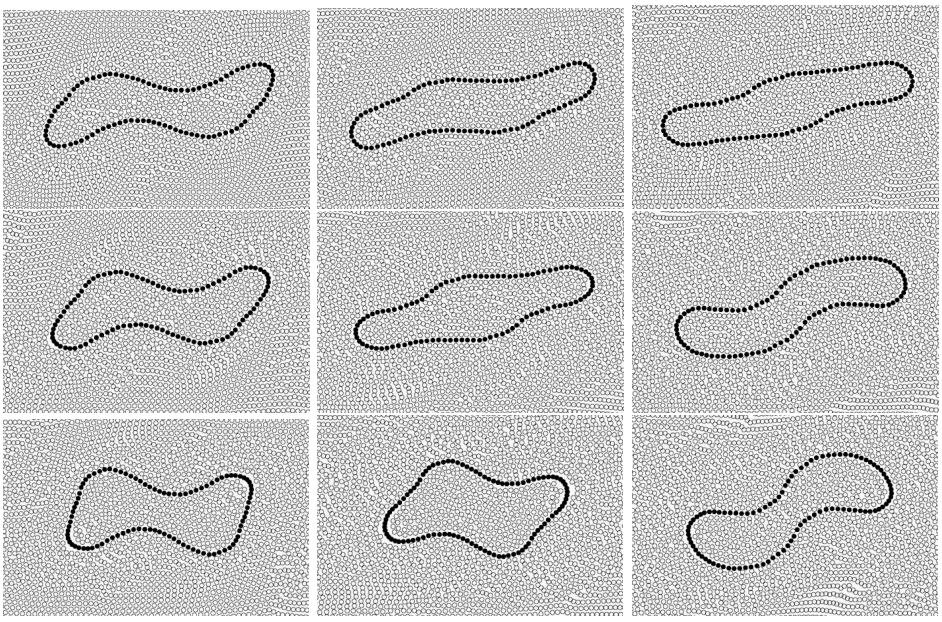

FIGURE 4. Effect of increasing the bending elasticity on cell deformation. $\hat{E}_B = 1.31 \times 10^{-2}$ (first row), 2.62×10^{-2} (second row) and 5.26×10^{-2} (third row) correspond to a bending elasticity 5, 10 and 20 times that of the real RBC. The three columns are for $kt = 3$, 5 and 7. G and C have the same value as in Fig. 3.

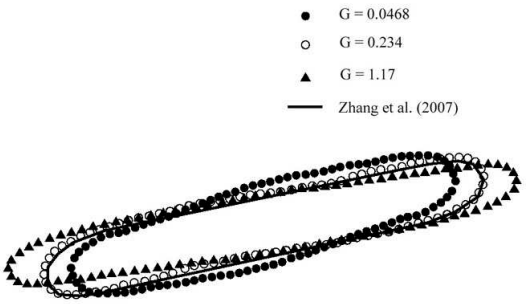

FIGURE 5. The steady shape of the RBC gets more elongated with increasing G values. All other dimensionless parameters have the same value as in Fig. 3. Note the quantitative agreement with the numerical result of Zhang *et al.* (2007) at $G = 0.234$, who used the immersed boundary method and a continuum model for the cell.

though the membrane constitutive equations differ between their study and ours, both used measured membrane properties to determine the model parameters. Thus, there is close agreement between the two studies. For instance, the evolution of the cell shape and the tank-treading motion in Fig. 3 are essentially identical to the predictions of Zhang *et al.* (2007). The steady-state cell shape, computed for identical dimensionless parameters, is in quantitative agreement between the two (Fig. 5). This serves as a validation of our particle-based model as well as our SPH algorithm.

Another feature of the simulation that can be quantitatively compared with previous work is the tank-treading frequency f, defined as the inverse of the period of tank treading. The data of Tran-Son-Tay *et al.* (1984) and Fischer (2007) show the frequency f, scaled by the shear rate k, to be in the range $f/k = 0.02$ – 0.038. Our results show a

higher frequency; for example, $f/k = 0.163$ for the conditions in Fig. 3. An obvious cause of this discrepancy is the two-dimensionality in our simulation. In a Stokes flow, a 2D solid cylinder rotates with a period of $2/k$ while a sphere has a much longer period $4\pi/k$ (Cox *et al.* 1968; Poe & Acrivos 1975). The factor of 2π is roughly the difference in f/k between our 2D computation and 3D measurements. In addition, our representation of the membrane is simplistic. Membrane viscosity may have also been a factor.

3.2. *Cell in Poiseuille flows*

Pressure-drive flow in a tube is a close analogy for blood flow in capillaries. Thus the deformation of an RBC in Poiseuille flow not only constitutes a benchmark problem for our model and numerical method, but has direct relevance to microcirculation. It is the latter connection that has motivated numerous previous studies. Perhaps the most profound discovery is that the red blood cell deforms into a characteristic parachute shape in order to traverse capillaries smaller than its undeformed diameter (Skalak & Branemark 1969). Numerical computations have mostly employed the continuum representation of an elastic shell enclosing a viscous liquid. Zarda *et al.* (1977) published one of the earliest finite-element computations of RBC deformation. Secomb (2003) modeled RBC deformation in a capillary using lubrication theory, for both axisymmetric and fully 3D geometries. The amount of deformation is studied as a function of the tube diameter and the flow velocity. Pozrikidis (2005*a*) computed the axisymmetric motion of a file of red blood cells in the Stokes regime using the boundary-integral method. The cell membrane was modeled by an elastic shell obeying the Skalak constitutive law (Skalak *et al.* 1973).

Against this backdrop, we test our particle-based model by computing the deformation of a initially biconcave RBC in a pressure-driven flow in a 2D channel. The channel width is $2.15a$, 7.7% wider than the diameter of the undeformed RBC, and its length is $10a$. The RBC is initially placed in the middle of the channel with its broad side facing the flow direction (Fig. 8), and a parabolic velocity field is imposed initially throughout the domain. For the two ends of the domain, periodic conditions are used such that particle exiting one end re-enters the other. The number of SPH particles is comparable with that for the shear-flow computations, and we adopt similar physical parameters based on experimental measurements of cell membrane moduli. For simplicity, we again assume equal viscosity for the cytoplasm and the suspending liquid.

Figure 6 depicts the deformation of an RBC in a capillary, with the dimensionless parameters being $C = 2 \times 10^4$, $G = 0.024$ and $\hat{E}_B = 1.97 \times 10^{-3}$. These values have been chosen to match those of Secomb (2003), who assumed a somewhat smaller bending modulus $E_B = 1.5 \times 10^{-19}$ N·m. The higher flow velocity in the middle of the channel causes the center of the cell to bulge forward. This counters and quickly overcomes the native curvature of the membrane in the front ($U_m t/a = 3.85$) and eventually leads to the 2D version of the parachute shape in steady state. Note that most of the deformation occurs within the first few cell radii that the cell center travels. Similar to the simulation in Fig. 3, the bending elasticity is weak and the cell deforms with the fluid more or less affinely. Since the parameters G and $\hat{E}_B$ were chosen to be consistent with real RBC properties and typical flow conditions in the capillary, the shape evolution in Fig. 6 being in general agreement with in vivo observations (Skalak & Branemark 1969, e.g.) is encouraging. One may also notice the slight top-bottom asymmetry in the cell shape. This is a numerical artifact due to updating the particle positions sequentially in an explicit scheme, and diminishes with reduced time step.

A more quantitative comparison is done in Fig. 7 with the numerical result of Secomb (2003). Both studies used the same dimensionless parameters G, $\hat{E}_B$, C and the same

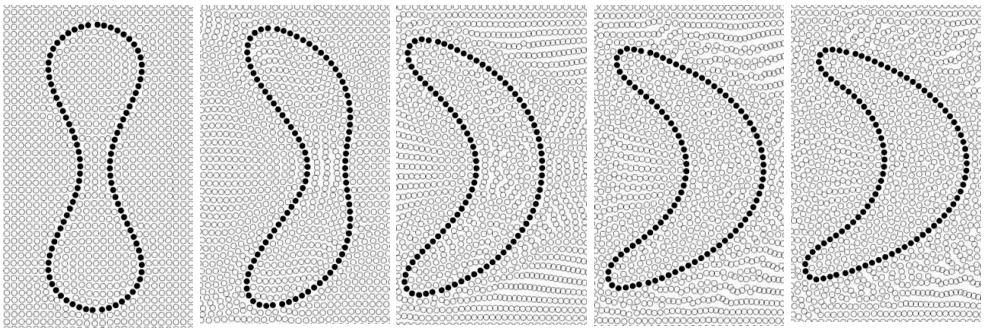

FIGURE 6. Deformation of a red blood cell in a Poiseuille flow. The flow is from left to right, and the five snapshots are taken at dimensionless time $U_m t/a = 0$, 1.28, 3.85, 6.40 and 8.95, the last approaching the steady state. Despite the considerable change in shape, the circumference of the cell has increased a mere 1.05% relative to the undeformed state.

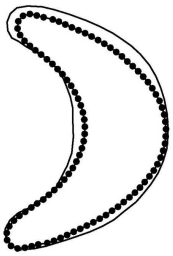

FIGURE 7. Comparison of the steady-state cell shape in a Poiseuille flow between our simulation (black dots) and the result of Secomb (2003) (continuous curve).

cell-to-tube diameter ratio. The steady-state RBC shape is in close agreement between the two. However, Secomb's cell appears to enclose more area than ours. This is a geometric effect. His calculation was for an axisymmetric cell while ours is planar. Thus, the conservation of membrane area corresponds to differing contour lengths in the plane. Besides, the membrane curvature is computed differently; the axisymmetric membrane has two principal curvature while our planar contour has one. Thus, the bending elasticity is represented differently in the two geometries, even though the material parameters are matched. Finally, Secomb (2003) used the viscoelastic Kelvin model for the membrane while we used the nonlinear elastic Skalak model. These factors have given rise to the small differences in Fig. 7.

We have also varied G and $\hat{E}_B$ from physiologically based values to explore their effects on the deformed RBC shape. As expected, greater G produces more deformation, with the parachute taking on a deeper dome shape (Fig. 8a). Since inertia is negligible, changing G can be visualized as changing the velocity and viscous shearing in the external flow, the direct cause of cell deformation. The effect of $\hat{E}_B$ is subtler. While smaller bending modulus leads to more pointed ends at the edge of the cell, the center also becomes thicker, and in a sense less deformed (Fig. 8b). In the undeformed resting shape, the cell has a "dimple" at the center. As the bending modulus is weakened, it becomes easier to override the innate concavity at the dimple. Thus, as the stronger shear near the channel walls produces narrow and pointed edges, the cytoplasm is squeezed into the central part and causes it to swell.

Finally, Fig. 9 shows a simulation of an RBC entering a contraction in the capillary. This geometry is relevant to both the microcirculatory network and recent studies of cell mechanics in microfluidic channels (Shelby *et al.* 2003; Yap & Kamm 2005*b*; Zhou *et al.*

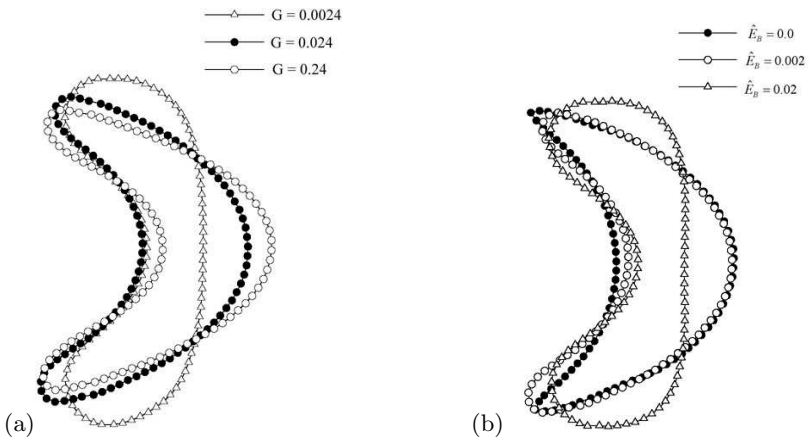

FIGURE 8. Effects of (a) G and (b) $\hat{E}_B$ on the steady state deformation of the RBC in a Poiseuille flow.

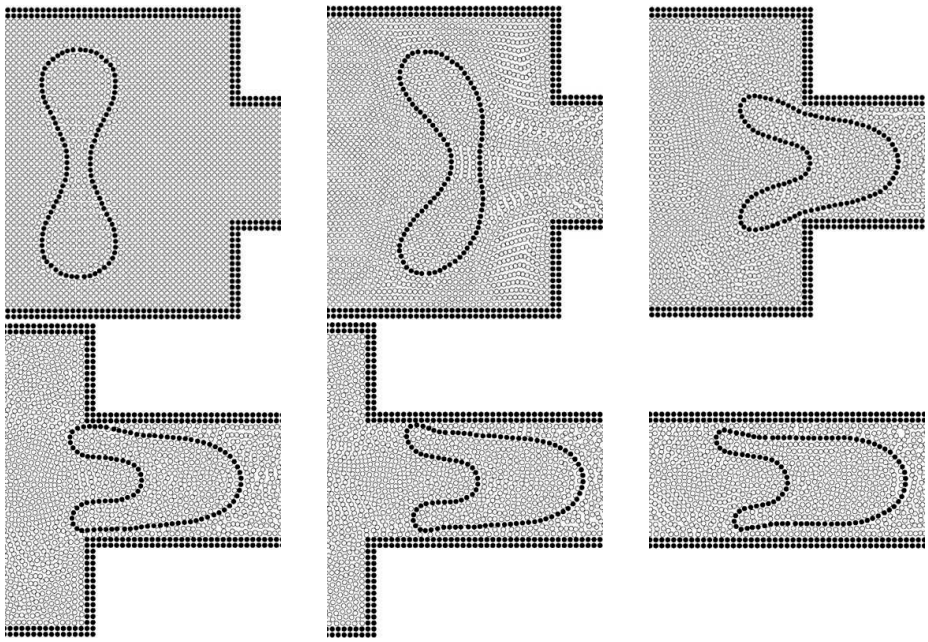

FIGURE 9. Deformation of a red blood cell as it goes through a contraction in the channel. The flow is from left to right. The width ratio between the narrow and wide channels is 0.4. Defined using the mean velocity in the wide channel, all flow and membrane parameters are the same as in Fig. 6. The snapshots are at dimensionless time $U_m t/a = 0$, 0.641, 1.60, 1.92, 2.24 and 2.88.

2007). The channel width is $2.15a$ in the upstream portion and $0.86a$ in the narrower part downstream. The extensional flow at the contraction deforms the cell into a boomerang. As the RBC enters the narrow tube, the two wings fold toward each other, increasing the bending of the membrane at the crotch in between. This causes the crotch to move back, shortening the wings and lengthening the front part of the RBC as it settles into a steady shape in the narrower tube. This steady shape bears a close resemblance to in vivo observations (Secomb *et al.* 2006, e.g.). Note that from the third frame ($U_m t/a = 1.60$) onward, the thin gap between the RBC and the corner or inner wall of the channel

contains only one layer of particles. Thus the local details of the flow are not adequately resolved in the computation.

4. Summary

We have proposed a particle-based model for the red blood cell as the basis for developing more general discrete-particle microstructural models for various cell types. The main goals of this study are to describe the model and present solutions on benchmark problems as validations. The cell membrane is represented by particles connected by nonlinear springs. A linear bending elasticity is implemented by using the local curvature. The inner and outer liquids are discretized by particles in the standard smoothed-particle-hydrodynamics (SPH) procedure. Thus, the model is an adaptation of SPH ideas; the particle-level physics is designed so as to produce the proper membrane elasticity. The particles are a numerical device for solving the partial differential equations as well as a vehicle for incorporating microscopic physics.

The model predictions of tank-treading in shear and the parachute shape in Poiseuille flows are in excellent agreement with experimental data and prior continuum-based computations. The model parameters are determined according to physiological measurements of cell viscosity and membrane elasticity, and no curve-fitting is involved. This agreement provides support for both the particle-based RBC model and the SPH-based numerical algorithm.

As the first step toward particle-based cellular modeling, this work employs a number of simplifications. For example, it is limited to two-dimensional geometry, and the cytoplasm is treated as a homogeneous liquid having the same viscosity as the suspending fluid. While such shortcomings do not hamper the objectives of the present study, which is mainly concerned with methodology and validation, they have to be remedied when such models are applied to explore new physical and physiological mechanisms in microcirculation.

A more ambitious generalization is to used discrete particles to represent intracellular microstructures, and probe their evolution in response to chemical and mechanical stimuli. If successful, this approach promises a unique route to understanding the microstructural remodeling inside the cell as a consequence of biochemical reactions on the one hand, and as the cause for pathological changes of cell property on the other.

Acknowledgment: We acknowledge support by the Petroleum Research Fund, the Canada Research Chair program, NSERC, CFI and NSFC (Grant Nos. 50390095, 20674051). Dr. Chunfeng Zhou provided assistance with the graphics in the paper, for which we are grateful. We thank the reviewer who suggested comparing the predicted tank-treading frequency with measurements.

REFERENCES

Bagchi, P. 2007 Mesoscale simulation of blood flow in small vessels. *Biophys. J.* **92**, 1858–1877.

Barthès-Biesel, D., Diaz, A. & Dhenin, E. 2002 Effect of constitutive laws for two-dimensional membranes on flow-induced capsule deformation. *J. Fluid Mech.* **460**, 211–222.

Batchelor, G. K. 1999 *An Introduction to Fluid Dynamics*. Cambridge: Cambridge University Press.

Boey, S., Boal, D. & Discher, D. 1998 Simulations of the erythrocyte cytoskeleton at large deformation. I. Microscopic models. *Biophys. J.* **75**, 1573–1583.

Boryczko, K., Dzwinel, W. & Yuen, D. A. 2003 Dynamical clustering of red blood cells in capillary vessels. *J. Mol. Model.* **9**, 16–33.

Bottino, D. C. 1998 Modeling viscoelastic networks and cell deformation in the context of the immersed boundary method. *J. Comput. Phys.* **147**, 86–113.

Cleary, P., Ha, J., Alguine, V. & Nguyen, T. 2002 Flow modelling in casting processes. *Appl. Math. Model.* **26**, 171–190.

Cox, R. G., Zia, I. Y. Z. & Mason, S. G. 1968 Particle motions in sheared. suspensions. XXV. Streamlines around cylinders and spheres. *J. Colloid Interface Sci.* **27**, 7–18.

Dong, C. & Skalak, R. 1992 Leukocyte deformability: finite element modeling of large viscoelastic deformation. *J. Theor. Biol.* **158**, 173–193.

Drury, J. & Dembo, M. 1999 Hydrodynamics of micropipette aspiration. *Biophys. J.* **76**, 110–128.

Dzwinel, W., Boryczko, K. & Yuen, D. A. 2003 A discrete-particle model of blood dynamics in capillary vessels. *J. Colloid Interface Sci.* **258**, 163–173.

Eggleton, C. D. & Popel, A. S. 1998 Large deformation of red blood cell ghosts in a simple shear flow. *Phys. Fluids* **10**, 1834–1845.

Evans, E. A. & Fung, Y. C. 1972 Improved measurements of the erythrocyte geometry. *Microvasc. Res.* **4**, 335–347.

Fischer, T. M. 2007 Tank-tread frequency of the red cell membrane: Dependence on the viscosity of the suspending medium. *Biophys. J.* **93**, 2553–2561.

Fischer, T. M., Stohr-Lissen, M. & Schmid-Schonbein, H. 1978 The red cell as a fluid droplet: tank tread-like motion of the human erythrocyte membrane in shear flow. *Science* **202**, 894–896.

Gingold, R. A. & Monaghan, J. J. 1977 Smoothed particle hydrodynamics: theory and application to non-spherical stars. *Mon. Not. Roy. Astron. Soc.* **181**, 375–389.

Herant, M., Marganski, W. & Dembo, M. 2003 The mechanics of neutrophils: Synthetic modeling of three experiments. *Biophys. J.* **84**, 3389–3413.

Hosseini, S. M. & Manifard, N. 2007 Presenting a modified SPH algorithm for numerical studies of fluid-structure interaction problems. *Int. J. Eng. Trans. B* **20**, 167–178.

Hosseini, S. M., Manzari, M. T. & Hannani, S. K. 2007 A fully explicit three-step SPH algorithm for simulation of non-Newtonian fluid flow. *Int. J. Num. Methods Heat Fluid Flow* **7**, 715–735.

Lee, G. Y. H. & Lim, C. T. 2007 Biomechanics approaches to studying human diseases. *Trends Biotech.* **25**, 111–118.

Li, J., Dao, M., Lim, C. & Suresh, S. 2005 Spectrin-level modeling of the cytoskeleton and optical tweezers stretching of the erythrocyte. *Biophys. J.* **88**, 3707–3719.

Li, X. & Sarkar, K. 2008 Front tracking simulation of deformation and buckling instability of a liquid capsule enclosed by an elastic membrane. *J. Comput. Phys.* **227**, 4998–5018.

Lim, C. T., Zhou, E. H. & Quek, S. T. 2006 Mechanical models for living cells - a review. *Journal of Biomechanics* **39**, 195–216.

Lucy, L. B. 1977 A numerical approach to the testing of the fission hypothesis. *Astron. J.* **82**, 1013–1024.

Monaghan, J. J. 1992 Smoothed particle hydrodynamics. *Ann. Rev. Astron. Astrophys.* **30**, 543–574.

Monaghan, J. J. 1994 SPH without a tensile instability. *J. Comput. Phys.* **159**, 290–311.

Monaghan, J. J. 2005 Smoothed particle hydrodynamics. *Rep. Prog. Phys.* **68**, 1703–1759.

Morris, J. P., Fox, P. J. & Zhu, Y. J. 1997 Modelling low Reynolds number incompressible flows using SPH. *J. Comput. Phys.* **136**, 214–226.

Nakamura, N., Tanaka, N. & Masuzawa, T. 2006 Improvement of model of red blood cell in analysis of blood flow using SPH method (in japanese). *Nihon Kikai Gakkai Kanto Shibu. Seimitsu Kogakkai Ibaragi Koenkai Koen Ronbunshu* pp. 45–46.

Pan, T.-W. & Wang, T. 2008 Dynamical simulation of red blood cell rheology in microvessels. *Int. J. Num. Anal. Model.* (submitted).

Pappu, V. & Bagchi, P. 2008 3D computational modeling and simulation of leukocyte rolling adhesion and deformation. *Comput. Biol. Med.* **38**, 738–753.

Pivkin, I. V. & Karniadakis, G. E. 2008 Accurate coarse-grained modeling of red blood cells. *Phys. Rev. Lett.* **101**, 118105.

Poe, G. G. & Acrivos, A. 1975 Closed-streamline flows past rotating single cylinders and spheres: inertia effects. *J. Fluid Mech.* **72**, 605–623.

Pozrikidis, C. 2003 Numerical simulation of the flow-induced deformation of red blood cells. *Ann. Biomed. Eng.* **31**, 1194–1205.

Pozrikidis, C. 2005*a* Axisymmetric motion of a file of red blood cells through capillaries. *Phys. Fluids* **17**, 031503.

Pozrikidis, C. 2005*b* Numerical simulation of cell motion in tube flow. *Ann. Biomed. Eng.* **33**, 165–178.

Secomb, T. W. 2003 Mechanics of red blood cells and blood flow in narrow tubes. In *Modeling and Simulation of Capsules and Biological Cells* (ed. C. Pozrikidis), chap. 4, pp. 163–191. London: Chapman and Hall.

Secomb, T. W., Hsu, R. & Pries, A. R. 2006 Tribology of capillary blood flow. *J. Eng. Tribol.* **220**, 767–774.

Secomb, T. W., Styp-Rekowska, B. & Pries, A. R. 2007 Two-dimensional simulation of red blood cell deformation and lateral migration in microvessels. *Ann. Biomed. Eng.* **35**, 755–765.

Shelby, J. P., White, J., Ganesan, K., Rathod, P. K. & Chiu, D. T. 2003 A microfluidic model for single-cell capillary obstruction by plasmodium falciparum-infected erythrocytes. *PNAS* **100**, 14618–14622.

Skalak, R. & Branemark, P.-I. 1969 Deformation of red blood cells in capillaries. *Science* **164**, 717–719.

Skalak, R., Özkaya, N. & Skalak, T. C. 1989 Biofluid mechanics. *Ann. Rev. Fluid Mech.* **21**, 167–204.

Skalak, R., Tozeren, A., Zarda, R. P. & Chien, S. 1973 Strain energy function of red blood cell membrane. *Biophys. J.* **13**, 245–264.

Stamenovic, D. & Coughlin, M. 2000 A quantitative model of cellular elasticity based on tensegrity. *J. Biomech. Eng.* **122**, 39–43.

Suresh, S. 2006 Mechanical response of human red blood cells in health and disease: some structure-property-function relationships. *J. Mater. Res.* **21**, 1871–1877.

Suresh, S., Spatz, J., Mills, J. P., Micoulet, A., Dao, M., Lim, C. T., Beil, M. & Seufferlein, T. 2005 Connections between single-cell biomechanics and human disease states: gastrointestinal cancer and malaria. *Acta Biomater.* **1**, 15–30.

Tanaka, N. & Takano, T. 2005 Microscopic-scale simulation of blood flow using sph method. *Int. J. Comput. Methods* **2**, 558–568.

Tran-Son-Tay, R., Sutera, S. P. & Rao, P. R. 1984 Determination of red blood cell membrane viscosity from rheoscopic observations of tank-treading motion. *Biophys. J.* **46**, 65–72.

Tsubota, K., Wada, S. & Yamaguchi, T. 2006*a* Particle method for computer simulation of red blood cell motion in blood flow. *Comput. Methods Progr. Biomed.* **83**, 139–146.

Tsubota, K., Wada, S. & Yamaguchi, T. 2006*b* Simulation study on effects of hematocrit on blood flow properties using particle method. *J. Biomech. Sci. Eng.* **1**, 159–170.

Yap, B. & Kamm, R. D. 2005*a* Cytoskeletal remodeling and cellular activation during deformation of neutrophils into narrow channels. *J. Appl. Physiol.* **99**, 2323–2330.

Yap, B. & Kamm, R. D. 2005*b* Mechanical deformation of neutrophils into narrow channels induces pseudopod projection and changes in biomechanical properties. *J. Appl. Physiol.* **98**, 1930–1939.

Yeung, A. & Evans, E. 1989 Cortical shell-liquid core model for passive flow of liquid-like spherical cells into micropipets. *Biophys. J.* **56**, 139–149.

Zarda, P. R., Chien, S. & Skalak, R. 1977 Interaction of viscous incompressible fluid with an elastic body. In *Computational Methods for Fluid-Solid Interaction Problems* (ed. T. L. Geers). New York: American Society of Mechanical Engineers.

Zhang, J., Johnson, P. & Popel, A. 2007 An immersed boundary lattice Boltzmann approach to simulate deformable liquid capsules and its application to microscopic blood flows. *Phys. Biol.* **4**, 285–295.

Zhou, C., Yue, P. & Feng, J. J. 2007 Simulation of neutrophil deformation and transport in capillaries using simple and compound drop models. *Ann. Biomed. Eng.* **35**, 766–780.

Zhou, D. & Wagoner, R. H. 1995 Development and application of sheet-forming simulation. *J. Mater. Process. Tech.* **50**, 1–16.

Zhou, D., Yue, P. & Feng, J. J. 2008 Viscoelastic effects on drop deformation in a converging pipe flow. *J. Rheol.* **52**, 469–487.